J. Phys. D: Appl. Phys. **46** (2013) 245501 (8pp) doi:10.1088/0022-3727/46/24/245501

Electron radiography using a table-top laser-cluster plasma accelerator

G C Bussolino[1], A Faenov[2,3], A Giulietti[1], D Giulietti[1,4], P Koester[1], L Labate[1,4], T Levato[1,5,6], T Pikuz[2,3] and L A Gizzi[1,4]

[1] ILIL, Istituto Nazionale di Ottica, CNR, Via G. Moruzzi 1, Pisa, Italy
[2] Joint Institute for High Temperatures, Russian Academy of Science (RAS), 13-2, Izhorskaya st., Moscow 125412, Russia
[3] Quantum Beam Technology Directorate, Japan Atomic Energy Agency, 8-1-7 Umemidai, Kizugawa, Kyoto 619-0215, Japan
[4] INFN Sezione di Pisa, Largo Pontecorvo 3, 56127 Pisa, Italy
[5] Università di Roma 'Tor Vergata', Dipartimento Ingegneria Industriale, Via del Politecnico 1, 00133 Roma, Italy
[6] Fyzikální ústav AV ČR v.v.i., Na Slovance 2, 182 21 Praha 8, Czech Republic

E-mail: giancarlo.bussolino@ino.it

Received 21 December 2012, in final form 22 April 2013
Published 31 May 2013
Online at stacks.iop.org/JPhysD/46/245501

Abstract
We explore the use of a laser-based electron gun for applications in transmission electron radiography and microscopy at electron energies up to 2 MeV. This new approach holds the promise to overcome some limitations of existing conventional electron guns at high beam energies especially for ultrafast applications. Our laser-electron gun is based on titanium-sapphire, ultrashort pulse lasers to drive electron acceleration in a plasma. The focused laser pulse travels in a tailored Ar gas target and accelerates electrons to MeV energy in less than a millimetre. As a first application, we use this electron beam to perform contact transmission electron radiography of cm-scale thin and thick samples. We obtain transmission electron radiography of organic and inorganic dense objects over a field of view more than 50 mm wide. The images are well exposed and show details of both thick and thin samples. The spatial resolution for the current geometrical configuration was found to be approximately 60 μm and was limited by geometrical effects combined with the intrinsic detector resolution and diffusion in the sample.

(Some figures may appear in colour only in the online journal)

1. Introduction

Progress of medical and biological imaging using radiation and particle beams relies on the continuous innovation of both detection techniques and beam generators. Nowadays, in addition to 'conventional' transmission radiography and microscopy (which basically employ electrons up to a few hundreds of keV energy accelerated by electrostatic fields), advanced applications, such as ultrafast electron diffraction and microscopy, based on radio frequency (RF) driven linear accelerators, are actively studied.

An alternative electron acceleration technique based on the original concept of laser-plasma acceleration [1] exploits the latest generation of high-power lasers in place of standard RF techniques and is found to be a thousand times more effective than conventional electron accelerators [2] leading to very compact and efficient electron beam generators. Laser pulses are focused on small gas targets to produce a plasma and accelerate electrons to MeV energy in a few millimetres. Laser-plasma acceleration has seen a dramatic development in recent years [3–5] with many laboratories involved worldwide [6] and is now sufficiently mature to be considered for applications.

In the configuration investigated in detail in previous experiments at the Intense Laser Irradiation Laboratory (ILIL) at the National Institute of Optics (CNR-INO) in Pisa and described elsewhere [7, 8], the electron beam has physical and geometrical properties, which appear to be suitable for imaging

applications. In this paper, we will refer to this particular laser-plasma acceleration configuration as a *laser-electron gun*.

Driven by this and other applications of laser-plasma acceleration [9–13], concepts for the engineering of these laser-electron guns are already being developed and are expected to be available in the near future. In view of these considerations, it is timely to start performing laboratory applications using prototypes of laser-electron guns like the one currently available at ILIL. Among possible applications, electron radiography offers the possibility to explore both physical and geometrical properties of the electron beam produced by the laser-electron gun and has a significant potential impact [14] on imaging of dense objects including biological and medical diagnostics.

The peculiar advantage of our laser-electron gun in comparison with RF technology comes mainly from the very short bunch duration, originating from the very short duration of the driving laser pulse, down to a few tens of femtoseconds. These circumstances enable the possibility of performing time-resolved studies including electron radiography, as demonstrated in [15] for these kinds of sources. In fact, there is a growing interest in ultrafast electron sources for both microscopy and diffraction applications [16, 17] and laser-driven electron guns are attracting attention for their intrinsic femtosecond duration and for their virtually jitter-free synchronization when operating in pump and probe configuration.

In this paper, we briefly recall the basic working principle of a laser-electron gun and focus on the properties of the electron beam that are required for radiography. We then describe the set-up of our radiographic experiment and present the experimental results and the analysis with emphasis on physical and geometrical features. Finally, we discuss the perspective of this technique in view of achieving larger fields of view and better spatial resolution.

2. Methods and materials

As anticipated above, the laser-electron gun under consideration here is based on a laser-plasma accelerator that exploits the plasma wake-field acceleration principle, first proposed by Tajima and Dawson [1]. After early experimental demonstration of this principle [18] showing uncontrollable acceleration effects, recent studies with ultrashort pulse lasers [19] have finally demonstrated controllable plasma accelerations at very high energy with a very low beam divergence [3–5] and relatively small energy spread.

This technique is currently under investigation at ILIL within a programme of development of biological and medical applications of laser-accelerated electrons. A schematic layout of our experiment is shown in figure 1. The pulse of a high-intensity femtosecond laser, 40 fs in duration and 100 mJ in energy, is focused using a special reflective off-axis parabolic mirror on a pulsed cluster gas jet [8, 20] operated with argon at a backing pressure up to 50 bar. Argon gas jet is characterized by the presence of a significant number of Ar clusters, aggregates of up to 10^6 argon atoms, which enhance the laser–gas interaction [21]. In this case, current and divergence of the

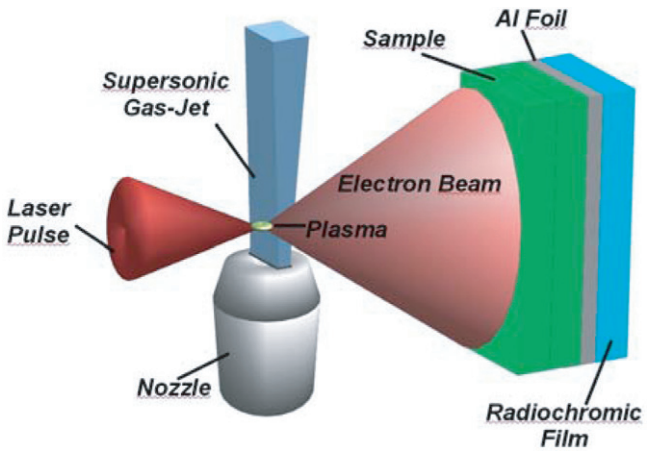

Figure 1. Schematic experiment layout.

accelerated electron beam are much larger than those in the case of interaction with lighter gases [3–5] and contribute to produce a significantly wider emission cone. As discussed below, both these properties are useful for electron radiography.

To explain the role of the clusters we carried out simulations of cluster formation in our gas jet, based on the model by Boldarev *et al* [22]. According to this study, optimized cluster formation in gas jet targets occurs at pressures between 40 and 50 bar with a maximum of cluster size and cluster concentration, and high atomic density of gas in the jet around 4×10^{19} cm^{-3}. According to our measurements, electron production in our configuration was found to occur at a gas jet pressure above 38 bar and stable operation of strong electron production was found at 46 bar, in good agreement with the Boldarev modelling. Under these conditions, the clusters size was 35 nm in radius with 5.5×10^6 atoms per cluster, with 12% of clusterized fraction (dryness of media was about 88%), very close to the maximum possible cluster size and concentration. These are the conditions used for our investigation on electron radiography.

The above observations strongly suggest that clusters play a key role in setting the conditions for optimized acceleration of electrons. However, a detailed description of the role of clusters in laser-plasma acceleration in general is still lacking.

A general description of laser-driven electron acceleration under our experimental conditions of relatively high density and moderate laser intensity shows that an important role is played by self-focusing of the laser pulse. In fact, the estimated critical power for relativistic self-focusing for electron densities above 3×10^{19} cm^{-3} is already below the TW level, which is below the actual power in our experimental set-up. Therefore, we expect self-focusing to always play a role in our laser-driven electron gun, as described by particle-in-cell numerical simulations [8] carried out using the code Aladyn [23].

In fact, as shown in figure 2, self-focusing is expected to occur approximately after 100 μm of laser propagation in the gas, leading to a significant increase in the effective intensity, at the levels required to drive laser acceleration in a strongly non-linear regime where a single accelerating cavity is finally formed [24], resembling the bubble regime.

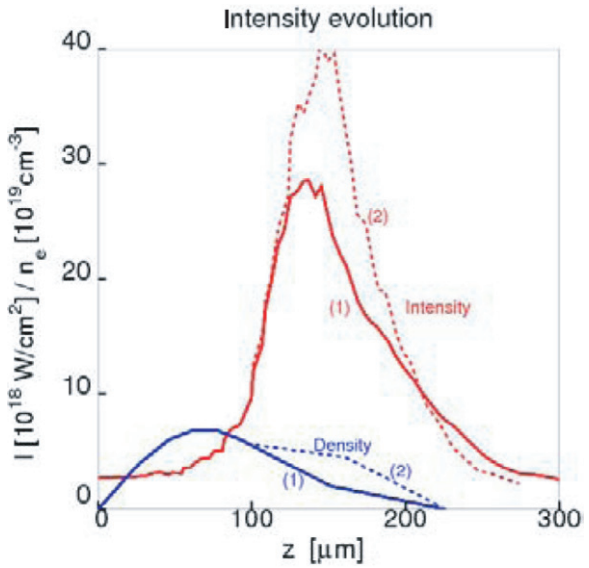

Figure 2. Evolution of the laser intensity for two density profiles (1, 2) showing that under our experimental conditions, a strong self-focusing occurs on a longitudinal scale length of less than 100 μm, leading to an increase of the local intensity exceeding one order of magnitude for both density profiles [8].

These considerations suggest that while self-focusing sets the basic conditions for acceleration to occur under our conditions, the presence of clusters makes this process become more effective at higher pressures, possibly stabilizing the injection of electrons in the accelerating cavity and leading to a higher charge in the accelerated bunch. In fact, our parameter scan ultimately shows stable production of a homogeneous electron beam only at the electron densities corresponding to optimized cluster formation.

The laser intensity in the focus and its position relative to the gas target are optimized to reach the conditions suitable for the generation of a high-energy electron beam. The process can be repeated ten times a second and is limited by the laser repetition rate and the gas jet target operation.

As shown schematically in figure 1, electrons are emitted in the forward direction relative to the direction of propagation of the laser pulse. Typically, each laser shot produces a bunch of electrons of approximately 12 ± 6 nC, with kinetic energy up to 2 MeV. Electrons are emitted in a cone with a divergence of typically 0.4 rad full aperture. The longitudinal extent of each electron bunch as it travels forward is very small, typically much less than 1 mm which, given the velocity very close to c, corresponds to a duration of less than 1 ps (1 ps $= 10^{-12}$ s). This electron beam can be represented as a thin layer of electrons travelling at the speed of light away from the laser–gas interaction point.

The energy distribution (above the detection limit of 1.5 MeV) shows a peak at 1.9 MeV and a width of 100%.

The energy of the accelerated electrons is suitable for radiography of biological samples with thickness of the order of the stopping range of the electrons in the sample material. The continuous slowing-down approximation (CSDA) range of electrons with kinetic energy of 1 MeV in water is about 4 mm. Therefore, all objects included in our samples were chosen with appropriate thickness. In the typical experimental configuration for electron radiography the sample is placed at a distance of 10 cm from the interaction point, where the beam has a transverse extent of more than 5 cm. In our case, at this distance, a trade-off exists between the maximum allowed size of the sample and the minimum intensity of the electron beam on the detector required to record an image with a good signal-to-noise (S/N) ratio. Depending on the sensitivity of the detector, the distance can be increased to expose larger samples. In our experiments, 30 consecutive laser shots are accumulated to obtain a single image.

As shown in figure 1, the radiographic image is taken using a sandwich of two radiochromic films (GAFCHROMIC® MD-55) arranged in a contact transmission configuration. We use radiochromic films as their response to electrons in the MeV range is matched to that of biological samples. Radiochromic films consist of a single or double layer of radiation-sensitive organic microcrystal monomers, on a thin polyester base with a transparent coating. When the active layer is exposed to ionizing radiation a reaction occurs which forms a blue coloured polymer. No processing is required to develop or fix the image. The colour of the exposed film turns to shades of blue whose optical density increases with increasing absorbed dose. Exposed films are then read by optical scanners using primarily light around 700 nm (red light) where the exposed films exhibit enhanced absorption.

The electron beam exhibits a high degree of local uniformity in the transverse dimension, as shown by the images of figure 3(a) obtained with a LANEX screen used to analyse the beam shape at the position of the sample. Figure 3(b) shows a lineout of the fluorescence intensity, taken along the line marked in figure 3(a). According to this plot, the intensity of the electron beam has a smooth variation across the field of view with no hot spots or other small-scale structures. This pattern is qualitatively reproducible from shot to shot. Accumulation of over 30 shots used in our measurements enabled us to increase the uniformity of irradiation of the sample up to the level of a few per cent.

One of the most important parameters for the qualification of radiographic imaging is the spatial resolution. This is, in general, given by the point spread function [25], namely the image of a point-like, perfectly opaque object. A more practical way to characterize the resolution of a radiological imaging system is to derive the modulation transfer function (MTF) from the Fourier transform of the line spread function (LSF). The latter can be easily obtained from the so-called edge spread function (ESF), which is obtained experimentally from the image of a sharp and opaque edge-like object and by extracting a lineout profile across the edge. The LSF is then obtained from the derivative of the ESF. This can be performed numerically using the actual data of the ESF profile plot. Alternatively, a fit of the profile plot data with an analytical function can be used and the LSF obtained from the derivative of the analytical ESF curve. Using this procedure, we will show that, compared with similar studies [14, 26], the resolution of the images presented here exhibits an improved performance.

We will also discuss limitations of the resolution in our particular configuration. In fact, the spatial resolution may be

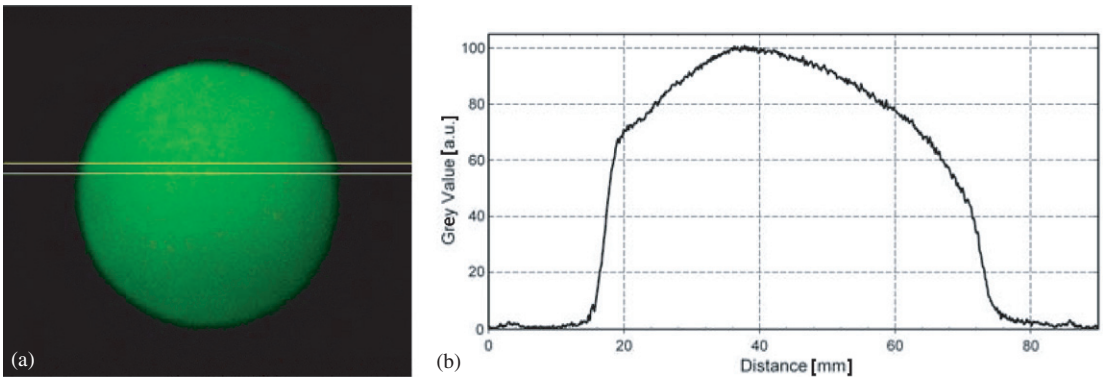

Figure 3. (*a*) Electron source image. (*b*) Profile taken along the line marked in figure 3(*a*).

Figure 4. (*a*) First sample and (*b*) second sample (real dimensions for both samples are 45 mm × 77 mm).

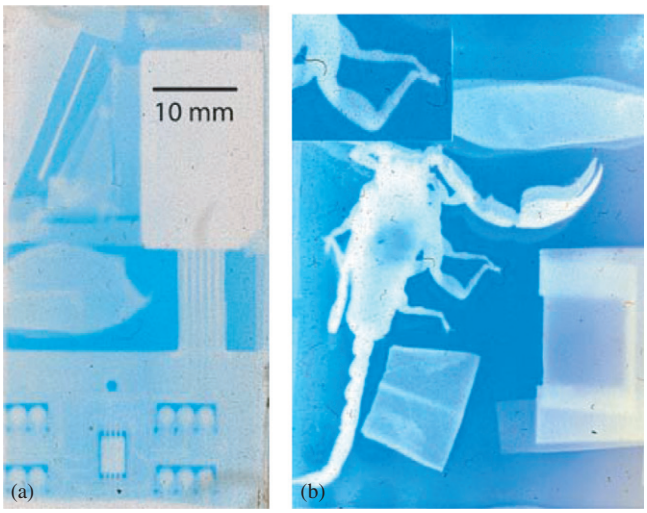

Figure 5. Electron radiography of the two used samples. (*a*) First: 34 mm × 63 mm; (*b*) second: 35 mm × 48 mm.

limited by several factors, including the detector resolution, the finite source size and the scanning/digitization error. As we will see in our case, most of the contribution will come from the detector resolution, the other contributions being negligibly small.

Another important parameter for the characterization of a radiological imaging system is the source intensity required to obtain a readable image, which ultimately determines the dose absorbed in the sample. Although this paper will mainly focus on the discussion of spatial resolution and field of view, some information will also be given below on the dose.

Finally, important information to complete the characterization of a radiological imaging system is related to the physical response of the object to the specific radiation, which ultimately sets the sensitivity of the system to the inner structure of the sample. It is well known that, in the case of electrons in the range of a few MeV, energy loss occurs mainly via ionization processes. This makes electron radiography sensitive to the (areal) density distribution of the object. Also, since the energy loss rate increases with a weak (logarithmic) dependence on the initial electron energy, it can be considered approximately constant over the range below 2 MeV, thus relaxing the constraint on the energy distribution of the electrons used for imaging. Incidentally, this circumstance is particularly favourable for our laser-electron gun which, in contrast with conventional high-energy electron guns, produces more electrons with a relatively broad energy spectrum. Therefore, given the weak sensitivity to electron energy spread, there is no need to make a selection of electron energy in the <2 MeV range and all electrons can be sent on the sample and contribute to the image.

In order to test the radiographic system parameters, including resolution and sensitivity to the areal density distribution, two samples with known different material compositions, thicknesses and spatial details were carefully prepared to be imaged by our system using both organic and inorganic objects. The first sample (see figure 4(*a*)) consisted of an electronic component (integrated circuit), two leaves, three Al foils of 13 μm thickness and a glass fibre. The second sample (see figure 4(*b*)) included a scorpion, two leaves, an electronic integrated circuit, a tantalum thin foil (5 μm in thickness) and two tungsten fine wires of 20 μm diameter.

A high-definition flatbed colour image scanner was used, in transmission mode, to analyse the exposed films. The use of these kinds of scanners is common in the readout of radiochromic films [27]. The scanner model adopted in this case was the 'Epson Perfection V600 Photo Scanner' with a hardware resolution of 6400 × 9600 dpi (dots per inch) and

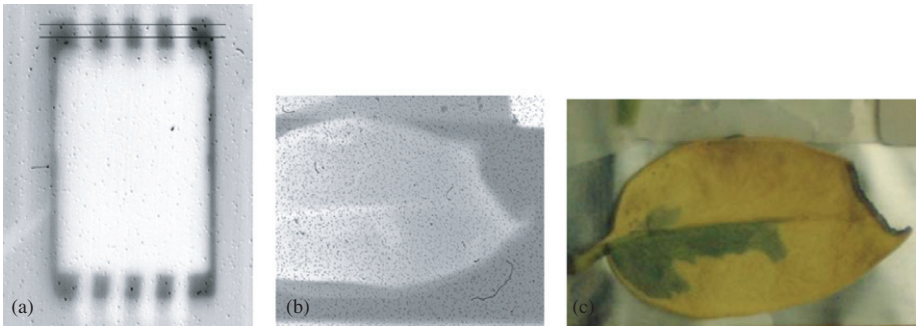

Figure 6. Details from the first sample. (*a*) 6 mm × 7 mm electron radiograph of a chip. (*b*) 18 mm × 15 mm electron radiograph of a two-coloured leaf. (*c*) Photo of a two-coloured leaf having length of 20 mm and height of 10 mm.

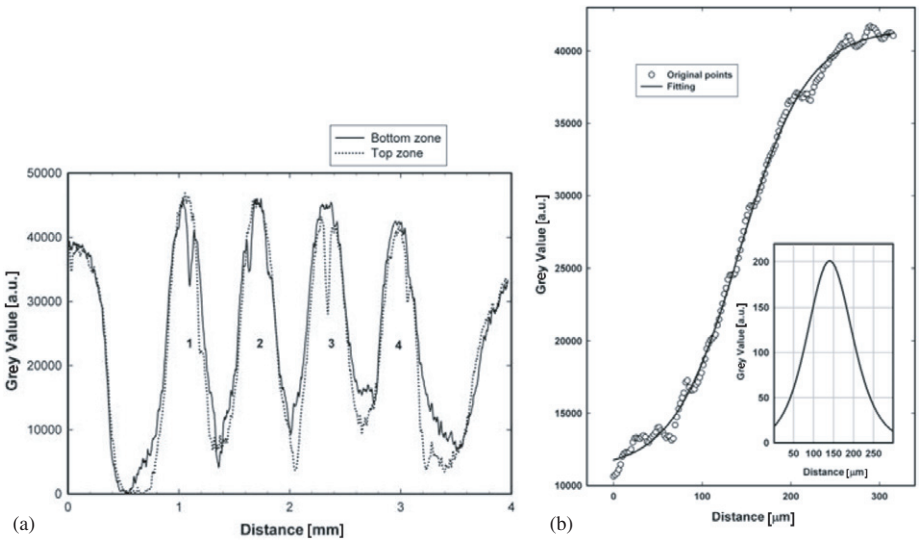

Figure 7. Printed circuit in the first sample. (*a*) Lineouts taken along the lines marked in figure 6(*a*). (*b*) Slope across the edge of pin no 4 (ESF) with the line transfer function (FWHM 150 μm) in the inset.

a true optical resolution of 6400 dpi. The colour depth for this model is 48 bit (16 bit per channel RGB) and the optical density range is 3.4. This last parameter is very important to understand how the scanner is able to adapt to the entire range of exposure levels of the film. The light source adopted by the scanner is 'ReadyScan® LED technology'. The film was positioned at the centre of the scan area in order to minimize possible inhomogeneities in the scanner response and oriented in landscape mode (scanning direction recommended by the film manufacturer). Images were acquired with red, green and blue colour components (RGB), using the 'Epson Scan' software package in professional mode. Data extracted from the scanner were stored in the uncompressed tagged image format (TIFF). As expected from the spectral response curve of the radiochromic films [28], inspection of the red channel showed the highest sensitivity and then gave the best information about the irradiation of the sample, particularly for the determination of the best spatial resolution.

3. Results and discussion

The 'overview' scans of the radiographic images corresponding to both samples of figures 4(*a*) and (*b*) are shown in figures 5(*a*) and (*b*), where the entire exposed films are shown. Under these conditions the estimated absorbed dose for each shot is of the order of 0.5 Gy. In the upper left corner of figure 5(*b*) a magnified image of a detail of the scorpion's legs is also shown. All other objects included in the sample are also clearly visible, including the three Al foils (13 μm in thickness from the first sample) in the upper left part of figure 5(*a*).

Additional high-resolution scans of details of different films provide further measure of the sensitivity and of the high-resolution capabilities of the system. Figure 6(*a*) shows the image of a small electronic integrated circuit included in the first sample. Figure 6(*b*) shows a detail of a leaf again from the first sample, where some local structures can be clearly seen. These details correspond to a region actually visible on the sample, as shown by the picture of figure 6(*c*) where a small green chlorophyll-rich area is still visible in an otherwise dried, yellow tissue. A comparison of the electron radiograph (figure 6(*b*)) with the original leaf photo (figure 6(*c*)) shows that the green region has a higher absorption than the surrounding yellow region. This difference is likely to be due to the presence of water in the green region, which increases the areal density compared with the dried yellow region. This is a clear indication of sensitivity of electron imaging to the chemical or structural differences in our sample qualitatively similar to

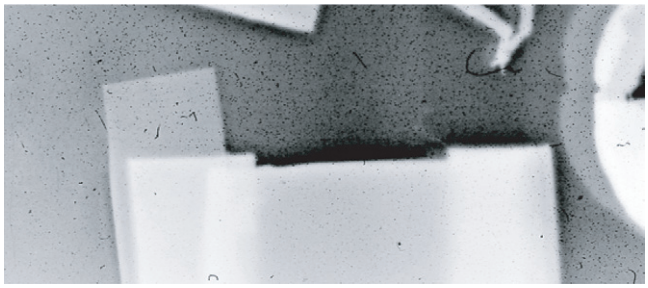

Figure 8. 13 mm × 29 mm electron radiograph of the tantalum foil (particularly from the second sample and red channel only).

that obtained using secondary x-rays produced by laser-plasma sources [29–31].

Among the different details of the images, we select small regions that can be used to extract the information on the spatial resolution. As a first attempt, we focus on the details of the integrated circuit consisting of the pins of the integrated circuit, as shown in the magnified image of figure 6(*a*).

Lineouts taken along the lines marked in figure 6(*a*) are shown in figure 7(*a*). Assuming that the edges of the pins can be considered sufficiently sharp and the pins themselves sufficiently opaque, we can obtain information on the spatial resolution from the slope of the lineout across one of these edges. The slope across the edge of pin no 4 is plotted separately in figure 7(*b*) and corresponds to the ESF discussed above. According to this plot and to the definition of ESF, we obtain the line transfer function of the inset of figure 7(*b*) with an FWHM of 150 μm. However, this result can be affected by the quality of the edge considered in the images, which, after a careful analysis, reveals a round shape which may contribute to the smoothing of the profile of figure 7(*b*).

As an alternative, we consider the edge of a 5 μm thick tantalum foil shown in figure 8 taking the red channel of the radiochromic scanned image.

The corresponding ESF is given by the lineout shown in figure 9 where the circles represent the original lineout obtained on the edge, while the solid curve represents a fitting with a 'Rodbard' function:

$$f = d + \frac{a - d}{1 + (x/c)^b} \tag{1}$$

where a, b, c and d could be determined with the best fit (solid line in figure 9) of the given experimental data (circles in figure 9). The fit quality index R^2 in this case is 0.9980. The derivative of this edge transfer function is shown in the inset of figure 9 and gives an LSF with an FWHM of 130 μm.

A similar result is found in different positions across the edge of the tantalum foil, as shown in figure 10. The plot of figure 10 shows the ESF taken at a different position across the edge.

This analysis yields an FWHM of 110 μm for the LSF. In order to further check the robustness of our analysis against the choice of the fitting function, we assumed a Gaussian LSF for which the resulting RMS width can be obtained from the parameter d of the well-known error function:

$$f = a + \frac{b}{2}\left(1 + \mathrm{erf}\frac{c(x - c)}{(\sqrt{2}d)}\right) \tag{2}$$

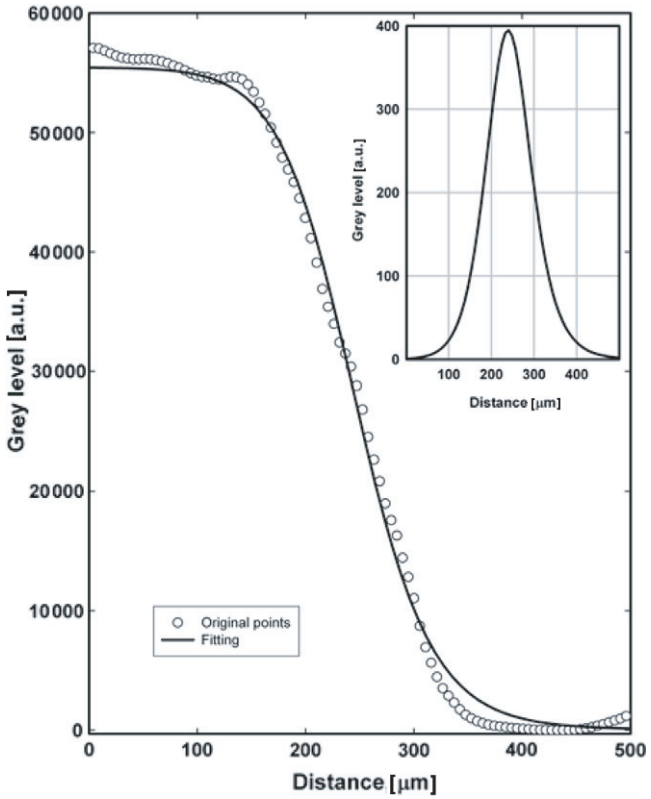

Figure 9. Lineout of the ESF for edge of a 5 μm thick tantalum foil (circles represent the original lineout while the solid curve represents a fitting with a Rodbard function with the best fit of the given experimental data). The derivative of this edge transfer function is shown in the inset and gives an LSF with an FWHM of 130 μm.

The result of this new fitting, taking the same experimental data included in figure 9, is shown in figure 11 and the fit quality index R^2 in this case is 0.9987. This procedure ultimately gives a spatial resolution of 60 μm, which is a remarkably good resolution for a 5 cm field of view used in our case. Also, as we will see below, this value can be further improved by adopting different detection techniques.

In fact, as anticipated above, the ultimate spatial resolution is set by several parameters, and the final result will be a convolution of all these components. In our case, the finite source effect due to the source size is negligible because of the contact imaging geometry. Incidentally, we point out here that the electron source size in the case of laser-electron guns is anyway very small [32] typically of the order of 10 μm and, in principle, projection imaging could also be considered and will be explored in future studies. As for the digitization error, taking into account the scanner resolution of 6400 dpi we have a pixel size on the image of less than 4 μm. Assuming sampling theory considerations we conclude that we can easily reconstruct details of the image of approximately three times the pixel size, which yields 12 μm resolution limits. As for the detector resolution, in the case of radiochromic films used in our set-up, the intrinsic resolution is very high, typically of the order of 1 μm or less. However, depending on the radiation and its penetration properties, exposure of the entire thickness of the sensitive layers takes place.

In our case, we expect that the overall spatial resolution for an MD-55 film is not limited by the scanner resolution, but is

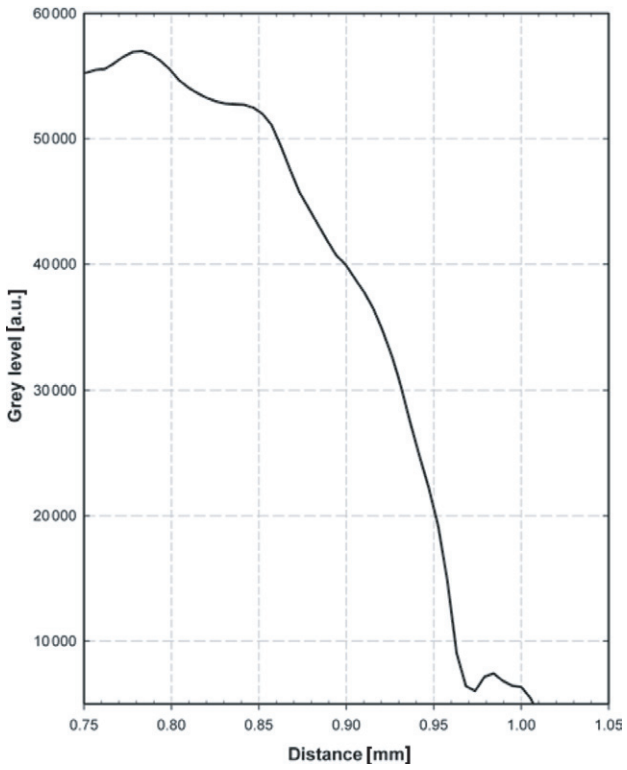

Figure 10. Spatial resolution determination: LSF obtained from the derivative of the ESF taken at a different position across the edge (tantalum foil) with an FWHM of 110 μm for the LSF.

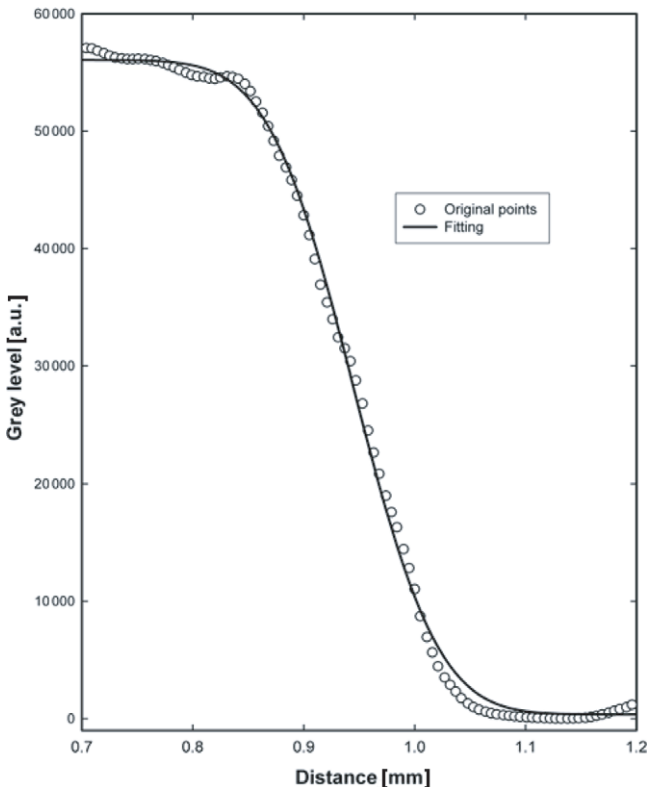

Figure 11. Fitting, taking the same experimental data included in figure 9, giving a spatial resolution of 60 μm (RMS width obtained from the error function).

due to the interaction of the electrons with the sample and with the detector material. In fact, the mean multiple scattering angle increases with increasing areal density and atomic number Z of the sample material and decreases with increasing electron energy. In our case, the resolution measurement was made using a 5 μm thick Ta foil, whereas the detector consists of a plastic material of about 200 μm thickness. On reaching the detector, electrons are first scattered when passing through the support layers of the radiochromic film. Monte Carlo simulation shows that for low-energy electrons (0.1–0.2 MeV) the spatial resolution results to be approximately 60 μm [33], which is comparable to the resolution of our images found using the step spread function above. However, a contribution to the angular spread is expected to come also from multiple scattering in the sample. In fact, in our case the contribution of multiple scattering in the 5 μm Ta foil is expected to be comparable to that in the detector. In general, Monte Carlo simulation can be used to obtain the detailed spatial distribution of the energy released by the electrons in the active layer of the detector after their passage through the sample. In this way, the optimum electron energy to obtain the highest possible spatial resolution can be found for a given sample.

These results are a first, quantitative demonstration of the performance of the laser-electron gun. Further studies are required to establish this technique to the standard required for biomedical applications. However, these results show that application to electron radiography is possible and gives encouraging results. Future work will be focused on several aspects that are not yet addressed at this prototyping stage. Among these, the possibility to further increase the field of view to allow electron radiography of even larger samples is probably the most interesting. In view of this, as anticipated above, we consider that, given the intrinsic geometrical properties of our laser-electron gun, a larger field of view can be easily obtained by placing the samples at larger distances from the source. This is, of course, done at the expense of the electron flux intensity in the sample and will therefore require higher intensity sources and/or higher sensitivity detectors. From the point of view of the source, the use of clusterized gas targets in the laser-electron gun, as shown here, is crucial. As discussed elsewhere, we are currently exploring this possibility using different gases with different clusterization dynamics and the preliminary experimental results achieved are encouraging [34]. In fact, with a higher flux it will also be possible to take radiographs in a single shot, avoiding any possible image blurring due to motion of the objects under test.

Another important parameter under investigation is the stability of the operation of the laser-electron gun parameters, including energy control and better shot-to-shot reproducibility and long-term operation. This will require improved control on both laser and target parameters. To reach the ultimate resolution, work is in progress to control the source in size, position and angle.

4. Conclusion

Laser-electron guns can be successfully applied to transmission electron radiography of thin and thick, cm-scale samples and, with the use of suitable detectors, this approach can

be extended to even larger field of view and higher electron energy, as required for thicker objects. Based on the conclusions of this study we estimate that with the use of currently available detection techniques, the resolution can be expected to easily reach the μm level. These results suggest that the availability of a new laser-driven electron source could be taken into account as a substitute for conventional RF electron guns for a cost-effective approach to high-resolution transmission electron microscopy at high electron energy and for configurations where multiple plasma sources are needed, making the capital investment (the laser) much more efficient and potentially even more affordable.

Acknowledgments

This work was carried out in the framework of the CNR High Field Photonics Unit (MD.P03.034).

The authors acknowledge financial support by the CNR funded Italian Research Network 'ELI-Italy' and by the INFN 'NTA-SITE' Project. AF and TP acknowledge financial support by INFN-FAI funds for participation in the experimental campaign at the ILIL.

The authors wish to thank Dr Maria Grazia Andreassi of the CNR Institute of Clinical Physiology for the careful and critical reading of our manuscript.

References

[1] Tajima T and Dawson J M 1979 *Phys. Rev. Lett.* **43** 267–70
[2] Esarey E and Sprangle P 1996 *IEEE Trans. Plasma Sci.* **24** 252
[3] Mangles S P D *et al* 2004 *Nature* **431** 535–8
[4] Geddes C G R, Toth Cs, van Tilborg J, Esarey E, Schroeder C B, Bruhwiler D, Nieter C, Cary J and Leemans W P 2004 *Nature* **431** 538–41
[5] Faure J, Glinec Y, Pukhov A, Kiselev S, Gordienko S, Lefebvre E, Rousseau J-P, Burgy F and Malka V 2004 *Nature* **431** 541–4
[6] ICUIL: The International Committee on Ultra-High Intensity Lasers homepage. www.icuil.org
[7] Gizzi L A, Cecchetti C A, Giulietti A, Giulietti D, Koester P, Labate L, Levato T and Pathak N 2011 *IEEE Trans. Plasma Sci.* **39** 2954–5
[8] Gizzi L A *et al* 2010 *Proc. 51st Workshop of the CHANNELING 2008 Conf. on Charged and Neutral Particles Channeling Phenomena (The Science and Culture Series—Physics) (Erice, Italy)* (Singapore: World Scientific) pp 495–501
[9] Giulietti A *et al* 2008 *Phys. Rev. Lett.* **101** 105002
[10] Faenov A Ya *et al* 2009 *Appl. Phys. Lett.* **95** 101107
[11] Cipiccia S, Reitsma A, Islam M R, Fiuza F, Martins J, Marti M, Silvia L and Jaroszynski D 2008 *35th EPS Conf. on Plasma Physics (Hersonissos, Greece)* vol 32D (ECA) P-1.144
[12] Gamucci A *et al* 2009 *2nd Int. Conf. on Ultraintense Laser Interaction Science; AIP Conf. Proc. (Frascati, Italy)* **1209** 39–42
[13] Murakami M *et al* 2008 *1st Int. Symp. on Laser-Driven Relativistic Plasmas Applied for Science, Industry, and Medicine; AIP Conf. Proc. (Kyoto, Japan)* **1024** 275–300
[14] Mangles S P D *et al* 2006 *Laser Part. Beams* **24** 185–90
[15] Schumaker W *et al* 2013 *Phys. Rev. Lett.* **110** 015003
[16] He Z -H, Thomas A G R, Beaurepaire B, Nees J A, Hou B, Malka V, Krushelnick K and Faure J 2013 *Appl. Phys. Lett.* **102** 064104
[17] Faure J, Rechatin C, Norlin A, Lifschitz A, Glinec Y and Malka V 2006 *Nature* **444** 737
[18] Modena A *et al* 2002 *Nature* **377** 606–8
[19] Strickland D and Mourou G 1985 *Opt. Commun.* **56** 219–21
[20] Cecchetti C A *et al* 2010 *2nd Int. Conf. on Ultra-Intense Laser Interaction Science; AIP Conf. Proc. (Frascati, Italy)* **1209** 19–22
[21] Faenov A Ya *et al* 2008 *Laser Part. Beams* **26** 69–82
[22] Boldarev A S, Gasilov V A, Faenov A Ya, Fukuda Y and Yamakawa K 2006 *Rev. Sci. Instrum.* **77** 083112
[23] Benedetti C *et al* 2008 *IEEE Trans. Plasma Sci.* **36** 1790
[24] Pukhov A and Meyer-ter-Vehn J 2002 *Appl. Phys.* B **74** 335
[25] Hasegawa B H 1991 *Medical Physics* 2nd edn (Madison, WI: Medical Physics Publishing)
[26] Ramanathan V *et al* 2010 *Phys. Rev. ST Accel. Beams* **13** 104701
[27] Butson M J, Cheung T and Yu P K 2005 *Phys. Med. Biol.* **50** N135-40
[28] Richter C, Pawelke J, Karsch L and Woithe 2009 *J. Med. Phys.* **36** 5506–14
[29] Koester P, Galimberti M, Giulietti A, Giulietti D, Gizzi L A, Labate L, Laville S and Suarez Garcia E 2005 *Appl. Phys.* B **80** 897–903
[30] Reale L *et al* 2006 *Microsc. Res. Tech.* **69** 666–74
[31] Reale L *et al* 2008 *Microsc. Res. Tech.* **71** 459–68
[32] Veisz L, Buck A, Nicolai M, Schmid K, Sears C M S, Sävert A, Mikhailova J M, Krausz F and Kaluza M C 2011 *Proc. SPIE* **8079** A05
[33] Galimberti M, Giulietti A, Giulietti D and Gizzi L A 2005 *Rev. Sci. Instrum.* **76** 053303
[34] Koester P *et al* 2013 arXiv:1301.3044